



Single-shot, mid-infrared ultrafast-laser-absorption-spectroscopy measurements of temperature, CO, NO and H₂O in HMX combustion gases

Vishnu Radhakrishna¹ · Ryan J. Tancin¹ · Garrett Mathews¹ · Christopher S. Goldenstein¹

Received: 14 September 2021 / Accepted: 17 November 2021 / Published online: 30 November 2021
© The Author(s), under exclusive licence to Springer-Verlag GmbH Germany, part of Springer Nature 2021

Abstract

This article describes the development of the first single-shot ultrafast-laser-absorption-spectroscopy (ULAS) diagnostic for simultaneous measurements of temperature and concentrations of CO, NO and H₂O in flames and aluminized fireballs of HMX (C₄H₈N₈O₈). Ultrashort (55 fs) pulses from a Ti:Sapphire oscillator emitting near 800 nm were amplified and converted into the mid-infrared through optical parametric amplification (OPA) at a repetition rate of 5 kHz. Ultimately, pulses with a spectral bandwidth of $\approx 600 \text{ cm}^{-1}$ centered near $4.9 \mu\text{m}$ were utilized in combination with a mid-infrared spectrograph to measure absorbance spectra of CO, NO, and H₂O across a 30 nm bandwidth with a spectral resolution of 0.3 nm. The gas temperature and species concentrations were determined by least-squares fitting simulated absorbance spectra to measured absorbance spectra. Measurements of temperature, CO, NO and H₂O were acquired in a HMX flame burning in air at atmospheric pressure and the measurements agree well with previously published results. Measurements were also acquired in fireballs of HMX with and without 16.7 wt% H-5 micro-aluminum. Time histories of temperature and species column densities are reported with a $1 - \sigma$ precision of 0.4% for temperature and 0.3% (CO), 0.6% (NO), and 0.5% (H₂O), and 95% confidence intervals (CI) of 2.5% for temperature and 2.5% (CO), 11% (NO), and 7% (H₂O), thereby demonstrating the ability of ULAS to provide high-fidelity, multi-parameter measurements in harsh combustion environments. The results indicate that the addition of the micron-aluminum increases the fireball peak temperature by $\approx 100 \text{ K}$ and leads to larger concentrations of CO. The addition of aluminum also increases the duration fireballs remain at elevated temperatures above 2000 K.

1 Introduction

Characterization of the physical and chemical properties of fireballs of energetic materials is essential to understand and control these highly dynamic combustion environments. The physical and chemical properties change rapidly within these fireballs and thus high-speed optical diagnostics are required to monitor the spatiotemporal evolution of chemistry within fireballs. Laser diagnostics can provide high-speed, quantitative, and non-intrusive measurements of various chemical species in combustion gases [1], thereby making them critical to further studies of fireballs. However, the harsh, multi-phase and turbulent combustion environment poses several challenges, such as optical transmission losses,

beamsteering, particulate scattering, and limited optical access.

Laser absorption spectroscopy (LAS) is a popular non-intrusive diagnostic which is capable of providing quantitative measurements of temperature, pressure, velocity and species concentrations in harsh combustion environments [1]. Narrowband, tunable lasers such as quantum-cascade lasers or diode lasers are often used in LAS diagnostics for detonation environments. For example, Murzyn et al. [2] made simultaneous measurements of pressure, temperature and H₂O concentration at 30 kHz in shock-heated air within a constant volume blast chamber. The authors utilized scanned-wavelength direct absorption with near-infrared tunable diode lasers (TDLs) and a rugged fiberoptic probe. Peng et al. [3] made time-resolved measurements of gas temperature and H₂O concentration at 20 kHz within the annulus of a hydrogen-air-fed rotating detonation engine (RDE) using scanned-wavelength-modulation spectroscopy near 2551 nm and 2482 nm. Later, Cassady et al. [4] obtained simultaneous measurements of temperature, and mole

✉ Vishnu Radhakrishna
radhakv@purdue.edu

¹ School of Mechanical Engineering, Purdue University, 585
Purdue Mall, West Lafayette, IN 47906, USA

fractions of H₂O, CO₂ and CO within the annulus of a H₂-C₂H₄-fueled RDE utilizing a four-color, single-ended, mid-infrared laser-absorption sensor. Water measurements were made using two tunable diode lasers centered near wavelengths of 2551 and 2482 nm, while CO₂ and CO measurements were acquired using an interband cascade laser (ICL) and a QCL centered near 4175 nm and 4854 nm, respectively. In addition, Rein et al. [5] acquired measurements of temperature, pressure and concentration of CO, CO₂, and N₂O in detonation gases of N₂O and C₃H₈ using three time-division-multiplexed QCLs. While highly effective in many scenarios, narrowband laser absorption techniques have a few drawbacks. For example, multiple lasers may be required to provide temperature measurements over a large temperature range [6] and the relatively small wavelength tuning often limits the range of pressures over which measurements can be obtained [1, 7]. Further, multiple lasers are typically required to provide simultaneous measurements of multiple species.

The development of both pulsed and continuous-wave broadband LAS diagnostics [8–13] has enabled LAS measurements to be acquired over 10's–1000's of cm⁻¹. For example, broadband, single-shot, dye-laser absorption measurements of Al and AlO were acquired at 10 Hz with a frequency bandwidth of 193 cm⁻¹ at 395 nm and 85 cm⁻¹ at 485 nm [14]. In addition, temperature measurements were acquired at 20 Hz via AlF and MgF [15] with bandwidths of 193–419 cm⁻¹ in the 227 and 268 nm regions, respectively, have been acquired in fireball environments. Carney et al. [16] made time-resolved absorption measurements (between 1335 and 1380 nm) of temperature and H₂O at 20 kHz using a fast, near-IR array and broadband light source to study the detonation of a high explosive. Later, Rein et al. [9] employed a MEMS-tunable vertical-cavity surface emitting laser (VCSEL) that scans in wavelength from 1330 to 1360 nm to measure temperature and H₂O at 100 kHz in the annulus of a hydrogen-air rotating detonation engine (RDE). More recently, Phillips et al. [17] acquired measurements of CO, CO₂, H₂O, and N₂O species concentrations at 100 Hz in post-detonation gases of explosives via high-resolution, broadband (2050–2300 cm⁻¹) measurements of absorbance spectra acquired using a swept-wavelength external-cavity QCL. While useful in many scenarios, such light sources are limited to only a few wavelength regions and, with a few exceptions (e.g., the MEMS-VCSEL), many broadband scanned-wavelength diagnostics do not provide a time-resolution suitable for resolving highly-transient combustion or detonation events.

To address these challenges, broadband LAS techniques leveraging ultrashort pulses to generate a supercontinuum at high repetition rates have also been developed. For example, Sanders [11] utilized a femtosecond-fiber-laser-pumped supercontinuum source along with a scanning

bandpass filter to provide temperature, H₂O, CO₂, C₂H₂, C₂H₆O measurements at 50 kHz using a spectral bandwidth of 1000 cm⁻¹ near 1450 nm. In addition, Blume and Wagner [12] utilized a supercontinuum laser to acquire measurements of CH₄ and temperature at 200 Hz via 110 cm⁻¹ of bandwidth near 1650 nm. Most recently, LuCurto et al. [18] utilized supercontinuum LAS to measure temperature and column densities of TiO and AlO in fireballs of metal/ammonium perchlorate at repetition rates up to 100 kHz. While useful, supercontinuum-based LAS diagnostics often require multi-shot averaging to achieve high SNR, thereby limiting their time resolution.

Alternatively, various researchers have also developed LAS diagnostics employing ultrafast lasers and a grating-based spectrometer to acquire broadband absorption measurements. For example, Zamkov et al. [19] studied the chemical reactions associated with flash heating of nanoenergetic materials using mid-infrared ultrafast (~200 fs pulses) spectroscopy in thin films. The laser system could be centered at wavelengths between 2.5 and 18 μm and generated pulses with an energy ranging from ~1 to ~30 μJ and a bandwidth of ~150 cm⁻¹. Bowlan et al. [20] made single-shot measurements to probe the shock-induced chemistry in two organic liquids using broadband (800–1400 cm⁻¹) mid-IR pulses generated at 150 fs and a mid-IR spectrometer. Regarding gas-phase diagnostics, Loparo et al. [21] utilized a pulsed, mid-infrared OPO emitting from 2.8 to 3.6 μm to measure multiple hydrocarbons (CH₄, C₂H₄, and C₂H₆) in both high-temperature reacting and non-reacting flows. In addition, Stauffer et al. [22] recently developed a technique called time-resolved, optically gated absorption (TOGA) spectroscopy to obtain background-free measurements of OH spectra. The authors used a Ti:Sapphire laser with amplification and frequency doubling processes to generate 100 fs pulses at a wavelength of 310 nm with a spectral bandwidth of 300 cm⁻¹.

Recently, we have developed and demonstrated an ultrafast-laser-absorption-spectroscopy (ULAS) diagnostic [23, 24] which is capable of providing broadband absorption measurements of temperature and species in combustion gases with sub-nanosecond time resolution. This manuscript presents a ULAS diagnostic which builds on our prior work [23–25] to provide the first single-shot ULAS measurements of temperature and multiple species (CO, NO, H₂O) simultaneously. This diagnostic is demonstrated with simultaneous measurements of temperature, CO, NO, and H₂O at a repetition rate of 5 kHz and with ultrafast time resolution in an HMX flame and fireballs of HMX with and without micro-aluminum, thereby demonstrating the ability of ULAS to provide multi-parameter measurements in harsh, particulated laden combustion gases.

2 Wavelength selection

Utilizing appropriate wavelengths is critical to the accuracy and precision of all LAS diagnostics. A 23 nm (9 cm^{-1}) wide band centered near $5.1 \mu\text{m}$ was utilized to provide simultaneous measurements of gas temperature, CO, NO, and H_2O via multiple absorption transitions in the fundamental vibration bands of CO, NO, and H_2O (ν_2 mode). This wavelength region was chosen for four primary reasons as described below.

1. **Magnitude of absorbance:** Strong fundamental band absorption lines were utilized to provide high signal to noise ratio (SNR) measurements in harsh HMX combustion environments. For all three species, the chosen wavelengths correspond to lines with a peak absorbance ≥ 0.1 at the nominal gas conditions ($T = 2700 \text{ K}$, $\chi_{\text{CO}} = 0.2$, $\chi_{\text{NO}} = 0.1$, $\chi_{\text{H}_2\text{O}} = 0.2$, $L = 10 \text{ cm}$) which is sufficient for high-SNR ULAS measurements given a typical absorbance noise level of 0.005.
2. **High lower-state energy (E''):** Lines with high E'' (typically $1000\text{--}9200 \text{ cm}^{-1}$) were used for two primary reasons. First, this enabled the diagnostic to avoid large absorption signals from ambient water vapor, which is critical due to the large path length ($\approx 3 \text{ m}$) of the optical setup through the lab air. For example, Zhou et al. [26] recommended utilizing H_2O lines with $E'' \geq 1700 \text{ cm}^{-1}$ to ensure that between 1000 and 2500 K the linestrength is three times its value at room temperature. Second, this reduces the amount of absorption that occurs in the colder boundary layers surrounding the flames and fireballs. As a result, the path-integrated temperature and species measurements are more representative of the conditions in the near-adiabatic core of these combustion environments [1].
3. **Wide range of E'' :** Utilizing lines with a wide range of E'' is required to enable sensitive and high-dynamic-range thermometry since this ensures that the absorbing state populations exhibit a widely varying temperature dependence [6, 27]. This is particularly important in high-temperature environments (e.g., flames) since temperature sensitivity decreases with increasing temperature. This diagnostic targets CO and H_2O lines which have a broad range of E'' (see Table 1), thereby meeting this requirement.
4. **Partially isolated lines:** To accurately determine the concentration of multiple species simultaneously, it is important to measure their absorbance spectra at wavelengths where the absorption lines of each species are at least partially isolated. This is to prevent errors in the spectroscopic database or model of one species from propagating into that of another species and, further, this

helps the least-squares fitting routine converge rapidly. The wavelength region used here consists of absorption lines belonging to CO, NO, and H_2O . While their absorption lines overlap significantly at some wavelengths, there are also wavelengths where the absorbance spectrum is dominated by lines belonging to a single species. This is illustrated in Fig. 1 which shows simulated absorbance spectra of CO, NO, and H_2O with and without instrument broadening at conditions representative of HMX fireballs. That being said, the required balance between isolated and overlapping lines is complex and additional research is needed to understand the the maximum pressure at which reliable multi-species measurements can be obtained with this diagnostic.

3 Absorption spectroscopy model and spectral-fitting routine

3.1 Multi-species absorption spectroscopy model

In LAS, laser light resonant with one or more absorption transitions is directed through a test gas and onto a photodetector or a spectrometer to measure the transmitted light intensity as a function of wavelength. The Beer–Lambert law, Eq. (1) can be used to relate the transmitted light

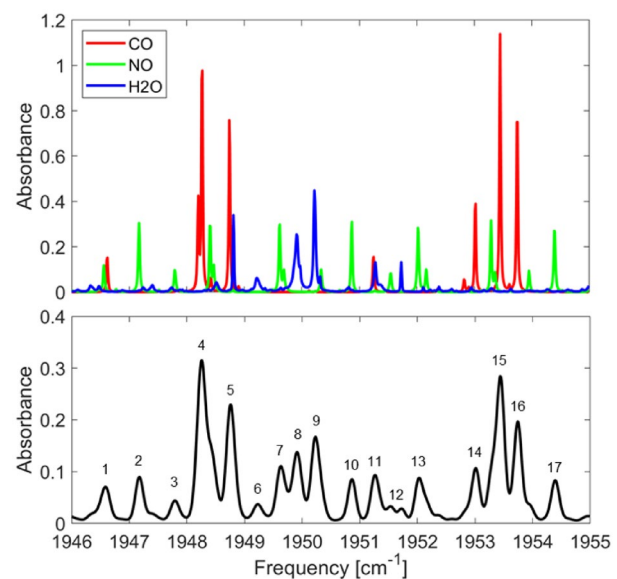


Fig. 1 High-resolution simulated absorbance of CO, NO and H_2O before convolution with the IRF (top); simulated total absorbance post-IRF convolution with a resolution of 0.3 nm (bottom). The simulation was conducted at $T = 2200 \text{ K}$, $\chi_{\text{CO}} = 0.05$, $\chi_{\text{NO}} = 0.025$, $\chi_{\text{H}_2\text{O}} = 0.08$, and with $L = 10 \text{ cm}$. The absorption features have been numbered and the pertinent spectroscopic parameters corresponding to each line are tabulated in Table 1

Table 1 Key spectroscopic parameters for measured absorption transitions

Feature	Species	ν_0 (cm ⁻¹)	E'' (cm ⁻¹)	$S(T_0)$ (cm ⁻² atm ⁻¹)
1	NO	1946.56 ^a	4135.925	8.604×10^{-8}
	CO	1946.616	7864.866	5.8×10^{-15}
2	NO	1947.17 ^a	960.979	0.1424
3	NO	1947.79 ^a	4307.67	3.732×10^{-8}
4	CO	1948.198, 1948.266	6370.168, 1615.552	7.362×10^{-12} , 2.104×10^{-6}
	NO	1948.40 ^a , 1948.47 ^a	1105.669, 4259.474	0.0703, 4.85×10^{-8}
5	CO	1948.743	4953.095	5.564×10^{-9}
	H ₂ O	1948.81 ^b	6402.154	1.0172×10^{-11}
6	H ₂ O	1949.217, 1949.250	4507.523, 1538.149	8.4111×10^{-9} , 0.0024
7	NO	1949.61 ^a , 1949.69 ^a	1042.809, 4433.584	0.0997 , 2.08×10^{-8}
8	H ₂ O	1949.870, 1949.91 ^b , 1949.974	4396.051, 4048.25, 8526.398	1.853×10^{-8} , 5.012×10^{-7} , 4.428×10^{-17}
9	H ₂ O	1950.229 ^b	2952.390	5.432×10^{-5}
	NO	1950.33 ^a	4386.273	2.69×10^{-8}
10	NO	1950.87 ^a	1189.413	0.0488
11	CO	1951.246	7760.682	9.296×10^{-15}
	H ₂ O	1951.278, 1951.382	4506.734, 5512.015	2.529×10^{-8} , 5.291×10^{-11}
12	NO	1951.54 ^a	4562.773	1.14×10^{-8}
	H ₂ O	1951.725	8350.971	2.581×10^{-16}
13	NO	1952.02 ^a , 1952.16 ^a	1127.965, 4516.316	0.0686 , 1.467×10^{-8}
14	CO	1952.824, 1953.016	9269.03, 6246.47	5.899×10^{-18} , 1.305×10^{-11}
15	NO	1953.29 ^a , 1953.36 ^a	1276.533, 4695.231	0.0332 , 6.149×10^{-9}
	CO	1953.449	3452.156	4.557×10^{-6}
16	CO	1953.745	4809.654	1.09×10^{-8}
	NO	1953.95 ^a	4649.601	7.875×10^{-9}
17	NO	1954.39 ^a	1216.447	0.0463

^aAverage line center frequency of the hyperfine split Λ -doubled lines. Corresponding lower-state energies are averages of the hyperfine split lambda-doubled lines and line strengths are the sum of the lines

^bA doublet

intensity to the spectral absorbance and, ultimately, thermodynamic properties of the gas.

$$\frac{I_t(\nu)}{I_0(\nu)} = \exp[-\alpha(\nu)]. \quad (1)$$

Here, I_t is the transmitted light intensity, I_0 is the incident light intensity, ν [cm⁻¹] is the optical frequency, and α is the spectral absorbance of the test gas which was modeled using Eq. (2).

$$\alpha(\nu) = \sum_i \sum_j S_{j,i}(T) \phi_{j,i}(\nu) P \chi_i L. \quad (2)$$

Here, $S_{j,i}(T)$ [cm⁻² atm⁻¹] is the linestrength of transition j of absorbing species i , $\phi_{j,i}$ [cm] is the lineshape function of the transition, P [atm] is the total pressure, χ_i is the mole fraction of absorbing species i , and L [cm] is the total path length through the absorbing gas. The lineshape of each transition

was modeled using a Voigt profile which accounts for Doppler and collisional broadening assuming they are independent. The number of lines simulated over the measured frequency range was limited by imposing a far-wing cut-off as done in Ref. [28]. Lines further than $\Delta\nu_{\text{cutoff}} = 20$ cm⁻¹ away from the minimum and maximum frequency of the measured spectra were ignored in the spectroscopic model.

The HITEMP2019 database was used for CO transitions, which is based upon the HITEMP2010 database [29] and includes updates largely based off of the work by Li et al. [30] along with improved line positions [31]. The HITEMP2019 database was also used for NO transitions [29, 32]; however, the HITEMP2010 database [29] was used for H₂O transitions with some adjustments. More specifically, for the H₂O doublet transitions at $\nu_0 = 1949.91$ ($J'' = K_c'' = 20$) and $\nu_0 = 1950.229$ ($J'' = 16$, $K_c'' = 15$), the values for γ_{self} , γ_{air} and n_{air} in the HITEMP2010 database were changed to 0.179 cm⁻¹ atm⁻¹, 0.01 cm⁻¹ atm⁻¹ and -0.16 , respectively. This was done based

on the work of Goldenstein and Hanson [33], who reported measured broadening parameters for H₂O doublets with similar J'' and K_c'' , albeit in a different vibration band, although this should not have a significant impact. This adjustment is further supported by the fact that this significantly reduced the residuals between measured and best-fit spectra in the combustion gases studied here.

To account for instrument broadening, transmitted intensity spectra were simulated at high spectral resolution using Eq. (3) and then convolved with the empirically derived instrument response function (Φ_{IRF}) of the spectrograph using Eq. (4).

$$I_{t,\text{sim,HR}}(\nu) = I_{0,\text{HR}}(\nu)e^{-\alpha_{\text{HR}}(\nu,T,P,\chi,L)}, \quad (3)$$

$$I_{t,\text{sim}}(\lambda) = \int_{-\infty}^{\infty} \Phi_{\text{IRF}}(\lambda - \tau)I_{t,\text{sim,HR}}(\tau)d\tau. \quad (4)$$

Here, $I_{t,\text{sim,HR}}$ is the high-resolution semi-empirical transmission spectrum, $I_{0,\text{HR}}$ is the high-resolution semi-empirical baseline intensity (obtained from up sampling a measurement of the baseline light intensity using linear interpolation), α_{HR} is the high-resolution absorbance spectrum which was calculated using Eq. (2) with a frequency increment of 0.0005 cm⁻¹, λ is the wavelength, τ is the convolution shift variable, and $I_{t,\text{sim}}$ is the instrument broadened, simulated transmitted light intensity. In the wavelength domain, the full-width at half-maximum (FWHM) of the IRF is constant, and therefore the convolution of intensity spectrum with the IRF is carried out in wavelength space. A Gaussian lineshape function was used to model Φ_{IRF} . Next, $I_{0,\text{HR}}$ was convolved with the IRF to create $I_{0,\text{sim}}$ and then Beer's law was used again to calculate the final simulated absorbance spectrum, α_{sim} , using Eq. (5) which was compared to measured absorbance spectra using the spectral-fitting routine described in Sect. 3.3.

$$\alpha_{\text{sim}}(\nu) = -\ln\left(\frac{I_{t,\text{sim}}(\nu)}{I_{0,\text{sim}}(\nu)}\right). \quad (5)$$

3.2 Collisional-broadening model

The collisional FWHM of each transition was calculated starting with Eq. (6), with various steps and approximations implemented to account for collisional-broadening coefficients varying between collision partners.

$$\Delta\nu_{c_{ji}} = 2P \sum_k \chi_k \gamma_{j,i-k}(T). \quad (6)$$

Here, $\Delta\nu_{c_{ji}}$ is the collisional FWHM of transition j of absorbing species i , the sum is executed over k collision partners, χ_k is the mole fraction of collision partner k , and $\gamma_{j,i-k}$ is the collisional-broadening coefficient of transition j of absorbing

species i colliding with species k . Due to the large number of collision partners in unknown proportions within a combustion gas, rigorously evaluating Eq. (6) is intractable. As a result, several assumptions were implemented to calculate the collisional FWHM of each transition with sufficient accuracy. Specifically, Eq. (7) was used to model the collisional FWHM of CO, NO, and H₂O lines since the HITEMP databases employed provide self-broadening and, for CO lines, H₂O-broadening coefficients.

$$\Delta\nu_{c_{j,\text{CO}}} = 2P\left[(1 - \chi_{\text{CO}} - \chi_{\text{H}_2\text{O}})\gamma_{j,\text{CO-bath}}(T) + \chi_{\text{CO}}\gamma_{j,\text{self}}(T) + \chi_{\text{H}_2\text{O}}\gamma_{j,\text{CO-H}_2\text{O}}(T)\right], \quad (7a)$$

$$\Delta\nu_{c_{j,\text{NO}}} = 2P\left[(1 - \chi_{\text{NO}})\gamma_{j,\text{NO-bath}}(T) + \chi_{\text{NO}}\gamma_{j,\text{self}}(T)\right], \quad (7b)$$

$$\Delta\nu_{c_{j,\text{H}_2\text{O}}} = 2P\left[(1 - \chi_{\text{H}_2\text{O}})\gamma_{j,\text{H}_2\text{O-bath}}(T) + \chi_{\text{H}_2\text{O}}\gamma_{j,\text{self}}(T)\right]. \quad (7c)$$

The self-broadening and air-broadening coefficients, as well as the temperature exponents for air-broadening for CO, NO and H₂O were all taken from the aforementioned HITEMP [29, 30, 32] databases. For CO, $\gamma_{\text{H}_2\text{O}}$ is available in the HITRAN2016 database for transitions with J'' up to 52; however, several of the CO transitions measured here correspond to higher J'' . As a result, for these transitions $\gamma_{\text{H}_2\text{O}}$ was obtained by extrapolating a two parameter exponential curve fit [(given by Eq. (8)] applied to $\gamma_{j,\text{CO-H}_2\text{O}}$ (296 K) vs J'' (see Fig. 2).

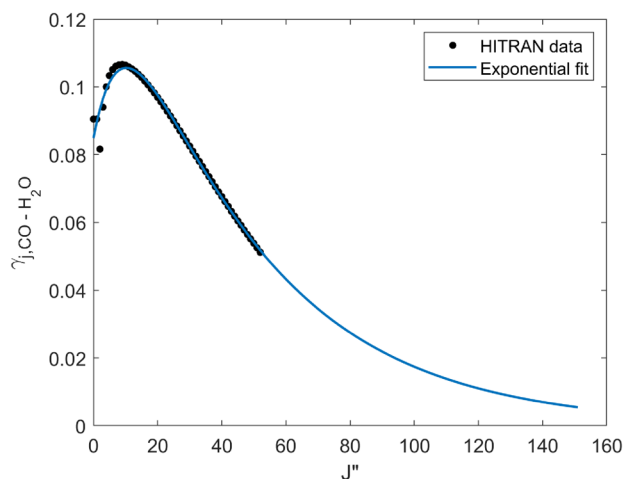


Fig. 2 Extrapolation of $\gamma_{j,\text{CO-H}_2\text{O}}$ at 296 K obtained from HITRAN database using a two parameter exponential fit to obtain $\gamma_{j,\text{CO-H}_2\text{O}}$ at 296 K for high J'' transitions located between 1900 and 2000 cm⁻¹

$$\gamma_{j,\text{CO-H}_2\text{O}}(296\text{ K}) = 0.1712 \exp[-0.02285J''] - 0.08635 \exp[-0.1036J''] \tag{8}$$

This exponential function was then extrapolated to calculate $\gamma_{j,\text{CO-H}_2\text{O}}(296\text{ K})$ for the higher- J'' CO lines measured here.

Collisional broadening due to the remaining collision partners in the combustion gas was accounted for via a single collisional-broadening coefficient for the bath gas ($\gamma_{j,i-\text{bath}}$) which was obtained using Eq. (9).

$$\gamma_{j,i-\text{bath}}(T) = \text{SF}_i \gamma_{j,i-\text{air}}(T) \tag{9}$$

Here $\gamma_{j,i-\text{air}}$ (taken from HITEMP databases) is the collisional-broadening coefficient for transition j of species i colliding with pseudo-species “air” (taken from HITEMP databases) and SF_i is a scaling factor which corrects for the fact that the bath gas consists of many other species, albeit, mostly diatomics. This scaling factor was estimated from an estimated composition of the combustion mixture and using scaling relations presented by Nair et al. [34] which were used to estimate collisional-broadening coefficients for collision partners which are not available in the HITRAN and HITEMP databases.

First, a series of equilibrium calculations were performed to estimate the major species expected in the HMX combustion bath gas. Constant temperature–pressure (TP) equilibrium simulations were conducted using NASA CEA for (a) pure HMX (100% fuel by weight) and (b) stoichiometric mixture of HMX (51% fuel by weight) and air. The latter was done to determine if air entrainment into fireballs significantly altered the effective broadening coefficient of the bath gas. For each case, calculations were performed for temperatures of 500 K, 1000 K, 1500 K, 2000 K, 2500 K, 2700 K, and 2900 K at a pressure of 1 atm. All species with an equilibrium mole fraction greater than 1×10^{-05} were then acknowledged in the calculations performed to estimate the effective collisional-broadening coefficient of the bath gas. This included the following species: CO, CO₂, H, H₂, H₂O, NO, N₂, O, O₂ and OH.

With the major species in the bath gas identified, appropriate values for SF_i were then found by calculating collisional-broadening coefficients of all collision partners using scaling relations (Eq. 10) and then performing a mole-fraction-weighted sum to determine $\gamma_{j,i-\text{bath}}$ [similar to Eq. (6)]. This approach to estimating collisional-broadening coefficients of a given species was presented by Nair et al. [34]; however, in the present work, we perform the scaling on $\gamma_{i-\text{air}}$ (instead of $\gamma_{i-\text{N}_2}$) out of convenience since $\gamma_{i-\text{air}}$ is tabulated in HITRAN or HITEMP for all the transitions studied here. The temperature exponent for each broadening coefficient was also calculated using a similar scaling method.

$$\gamma_{j,i-k}(T) = \gamma_{j,i-\text{air}}(T) \left(\frac{\sigma_{j,i-k}}{\sigma_{j,i-\text{air}}} \right)^2 \sqrt{\frac{\mu_{i-\text{air}}}{\mu_{i-k}}} \tag{10}$$

Here, $\sigma_{j,i-k}$ is the optical collision diameter for transition j of species i colliding with species k , $\sigma_{j,i-\text{air}}$ corresponds to collisions with the pseudo-species air, and μ_{i-k} is the reduced mass for species i and k . Equation (11) was used to calculate $\sigma_{j,i-k}$ and, similarly, Eq. (12) was used to calculate $\sigma_{j,i-\text{air}}$ according to intermolecular potential parameter combination rules developed for the Lennard–Jones 6–12 potential [35].

$$\sigma_{j,i-k} = \frac{1}{2}(\sigma_i + \sigma_k) \tag{11}$$

$$\begin{aligned} \sigma_{j,i-\text{air}} &= 0.78\sigma_{i-\text{N}_2} + 0.22\sigma_{i-\text{O}_2} \\ &= \frac{1}{2}(\sigma_i + 0.78\sigma_{\text{N}_2} + 0.22\sigma_{\text{O}_2}). \end{aligned} \tag{12}$$

Here σ_i and σ_k are the Lennard–Jones collision diameters of absorbing species i and collision partner k (taken from [36]). This approximation was implemented to overcome the fact that optical collision diameters are not available for many collision partners. While this transformation between optical collision diameter and Lennard–Jones collision diameters is not correct, the accuracy of Eq. (7) only relies on this transformation accurately capturing how the optical collision diameter scales between collision partners, as a result, this can often be approximated with reasonable accuracy from the ratio of Lennard–Jones collision diameters (with some notable exceptions, e.g., H₂O).

The reduced masses were calculated using Eq. (13).

$$\mu_{i-k} = \frac{m_i m_k}{m_i + m_k} \tag{13}$$

Here, m represents the atomic weight of a given species.

To determine SF_i , $\gamma_{j,i-\text{bath}}$ was calculated for various HMX combustion mixtures at several temperatures using the aforementioned scaling relations and Eq. (14).

$$\gamma_{j,i-\text{bath}}(T) = \sum_k \chi_k \gamma_{j,i-k}(T) \tag{14}$$

$\gamma_{j,i-\text{bath}}$ was then compared to $\gamma_{j,i-\text{air}}$ according to Eq. (9) to calculate SF_i . The mole fractions of each collision partner were estimated for various HMX combustion mixtures using constant-temperature–pressure (TP) equilibrium calculations. For example, Fig. 3 compares $\gamma_{j,\text{CO-bath}}$ calculated using either Eq. (14) (via scaling relations) or Eq. (9) with $\text{SF}_{\text{CO}} = 1.156$ for an HMX combustion gas in thermochemical equilibrium at 2700 K and 1 atm. The results indicate that the collisional-broadening coefficient of the bath gas can be accurately modeled by imposing a scaling factor on $\gamma_{j,\text{CO-air}}$ for a wide range of transitions (i.e., J''). The optimal value of SF_i was calculated for two mixtures: (i) pure HMX

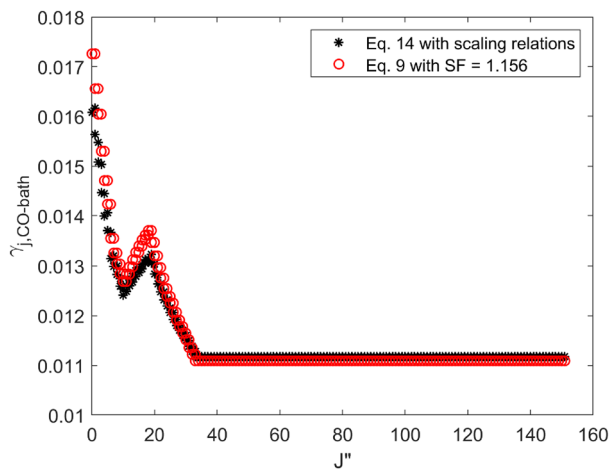


Fig. 3 $\gamma_{j,CO-bath}$ calculated using Eqs. (9) and (14)

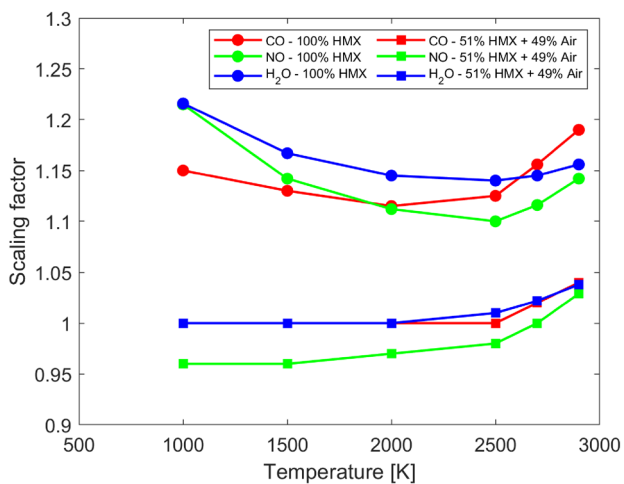


Fig. 4 Scaling factors for air broadening (SF_j) obtained for CO, NO and H_2O for the HMX combustion mixtures studied

and (ii) 51% HMX in air at several temperatures to estimate how SF_j may vary throughout a given fireball test. It was found that the addition of air into the mixture lowered the optimal values of SF_j and that temperature had a small effect. Figure 4 shows the scaling factor obtained for the two different mixtures at six different temperatures. It was noted that the scaling factors do not vary significantly between CO, NO, and H_2O for both mixtures investigated. The experimental data was processed twice using a scaling factor obtained from the mean of scaling factors for each mixture. The temperature and column density results obtained in each case did not differ significantly and, specifically, they were within each other's 95% confidence interval. Therefore the final model utilized a single scaling factor equal to 1.075 which was obtained by averaging all the values shown in Fig. 4.

3.3 Spectral-fitting routine

The gas temperature and absorbing-species column densities were determined from the measured absorbance spectra by employing a spectral-fitting routine. Figure 5 shows an example single-shot measurement of I_0 and I_t along with the measured and simulated best-fit absorbance spectrum. First, for each image of the laser pulse intensity, the most recent background image (acquired in between pulses) was subtracted off. The incident intensity spectrum was then calculated by averaging 200 recorded images of the incident laser pulse without the flame or fireball in the beam path. The averaging was done to reduce the noise in the I_0 spectrum. The background subtracted incident and transmitted intensities were then used to calculate the measured absorbance spectra using Beer's law. Next, the frequency axis of the measured absorbance spectra was determined by assigning the peak absorbance of four dominant absorbance features to correspond to their line-center frequency (obtained from a spectroscopic database). Next, linear interpolation was used to determine the frequency of each data point in the measured spectra. For fireball datasets, the spectral-fitting routine employed the absorption spectroscopy model described in Sect. 3.1 and the Levenberg–Marquardt algorithm with the following free parameters: the FWHM of the Gaussian instrument response function (Φ_{IRF}), temperature, mole fraction of each absorbing species (χ_{CO} , χ_{NO} , and χ_{H_2O}), a frequency shift variable, and two scaling factors for I_0 to account for shot-to-shot fluctuations. However, for the flame measurements, a single scaling factor on the collisional widths of each transition of individual species was floated instead of the FWHM of the IRF.

In flame experiments, beamsteering was insignificant and, as a result, the IRF FWHM was stable in time. In this case, the IRF FWHM was fixed to 0.3 nm in the spectral-fitting routine. Since the IRF FWHM was fixed, it was necessary to account for the unknown collision broadening via a scaling parameter to model the observed spectra with high accuracy. In comparison, in fireball experiments beamsteering was pronounced and the IRF FWHM clearly varied in time due to its impact on alignment on the spectrograph slit. Therefore, the IRF FWHM had to be floated in the spectral-fitting routine and was observed to vary from 0.3 to 0.38 nm. Floating the IRF FWHM ultimately can also account for unknown collisional broadening to some extent, due its impact on the measured lineshapes. Hence, the collisional broadening could not be varied in the spectroscopic model due to the IRF FWHM's similar impact on observed spectra. In future experiments, the spectrograph slit could be widened to mitigate the impact of beamsteering on the IRF FWHM, albeit at the cost of reducing spectral resolution.

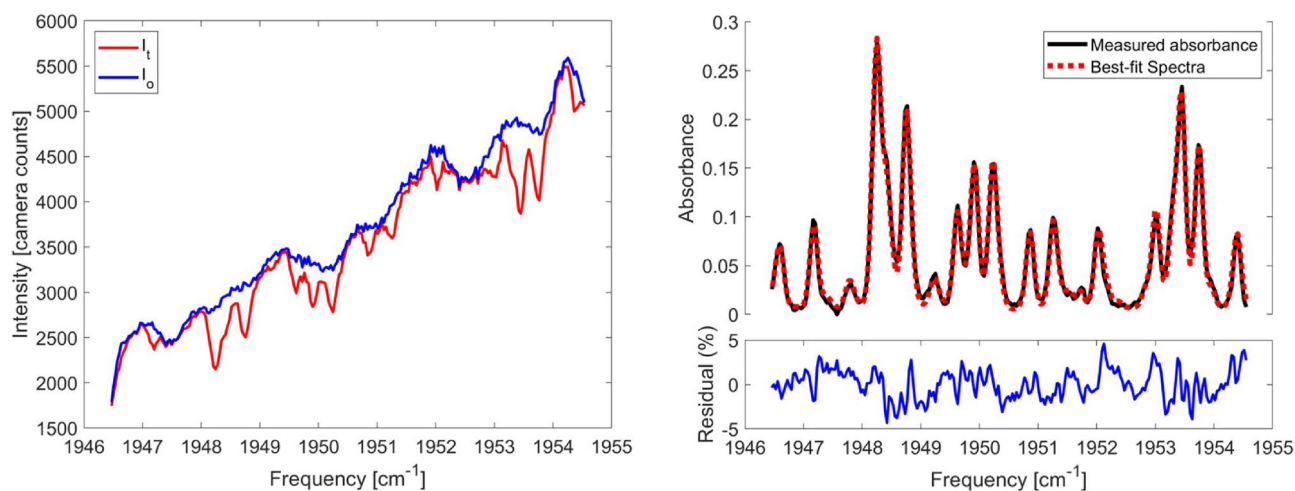


Fig. 5 Single-shot measurements of incident and transmitted intensity profiles (left) and measured absorbance with the simulated best-fit spectrum

3.4 Investigation of species-specific temperature measurements

A multi-temperature spectroscopic model, in addition to the single-temperature model [presented here in Eq. (2)] was also tested, wherein, temperatures for CO, NO and H₂O transitions were considered as individual parameters. Results showed that all three temperatures agreed well with each other in fireball measurements which suggests that all three species were present at similar temperatures along the line of sight or that the temperature along the line of sight was quasi-uniform. However, in the case of flame measurements, the temperatures of all three species were found to differ close to the propellant surface which is expected given the structure of HMX flames burning in air. In this case, further investigation is required to determine the advantages of a multi-temperature model which is the focus of our upcoming paper.

4 Experimental setup

4.1 Optical equipment

Figure 6 illustrates a CAD rendering of the ultrafast light source and experimental setup used in this work. The ultrafast light source consists of: a Ti:Sapphire oscillator (Coherent Mantis), a pulse shaper (femtoJock), a regenerative chirped-pulse amplifier (Coherent Legend Elite Duo) and an optical parametric amplifier (Coherent OPerA Solo) equipped with nonlinear difference-frequency-generation (NDFG) crystals. The oscillator generates ultrashort (55 fs) pulses centered near 800 nm at a repetition rate of 80 MHz.

The amplifier then selectively amplifies pulses to a pulse energy of 2 mJ at a repetition rate of 5 kHz. The amplified pulses are then directed to the OPA and NDFG package to produce ultrashort pulses centered at the desired wavelength. Ultimately this system can produce infrared pulses with a usable spectral bandwidth of ≈ 600 cm⁻¹ (i.e., approximately two times the pulse full-width at half maximum) at wavelengths from 2.5 to 16 μ m. For the experiments discussed here, pulses centered at 4.9 μ m with a pulse energy of 4.8 μ J (at the OPA output) were utilized.

The pulse train exiting the NDFG was directed into a periscope to raise the beam to the desired height. The pulses were then directed through a Rochon prism polarizer to achieve the desired pulse energy and prevent camera saturation. Next, the pulses were directed into a spatial filter consisting of: (1) a CaF₂ plano-convex lens with a 150 mm focal length, (2) a 100 μ m pinhole, and (3) a Si plano-convex lens ($f = 25.4$ mm, 2–5 μ m AR coating). The beam was focused on the pinhole, thereby filtering out the non-Gaussian components of the beam and then re-collimated by the Si plano-convex lens.

To characterize fireballs of HMX, the beam was directed through the test gas produced within our high pressure combustion chamber (HPCC) which is thoroughly described in [37]. The beam was then directed through a cylindrical lens (CaF₂, 75 mm focal length) to focus the beam in one dimension onto the slit of the spectrograph (Andor Shamrock 500i). A cylindrical lens was used to ensure that the spectrally dispersed pulses illuminate the entire focal plane array, thereby enabling multiple spectra to be averaged together to improve the signal-to-noise ratio of each single-shot measurement. A 300 lines/mm diffraction grating was used to provide a spectral resolution and bandwidth near 0.3 nm and 30 nm, respectively. A high-speed infrared camera

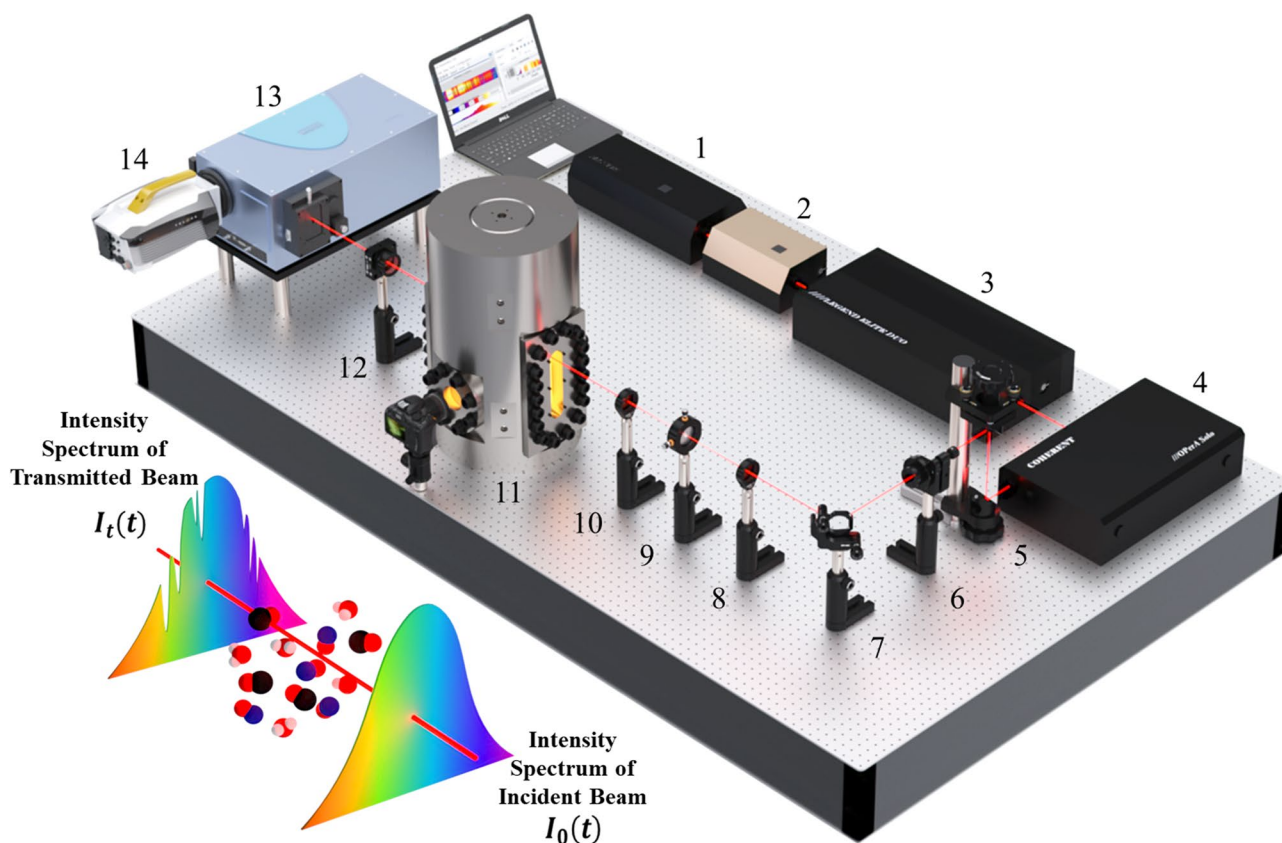


Fig. 6 CAD rendered 3D representation of the experimental setup used to create fireballs and perform ULAS measurements. (1) Ti:Sapphire laser. (2) Pulse shaper. (3) Pulse amplifier. (4) Optical parametric amplifier (OPA). (5) Periscope. (6) Polarizer. (7) Mirror.

(8) CaF₂ plano-convex lens ($f = 150$ mm). (9) 100 μm pinhole. (10) AR-coated Si plano-convex lens ($f = 25.4$ mm). (11) HPCC. (12) CaF₂ plano-convex cylindrical lens ($f = 75$ mm). (13) Imaging spectrometer. (14) High-speed IR camera

(Telops FAST-IR 2k) was used to image each pulse and to record background emission between each pulse. As a result, spectra were imaged at 10 kFPS with a 5 μs exposure time and a resolution of 44×320 pixels. Background emission recorded prior to each laser shot were subtracted off prior to processing each image of transmission spectra as mentioned previously.

To characterize HMX flames, the flame was placed adjacent to the spatial filter where the beam diameter was 1.2 mm. This was done to improve the spatial resolution. A multi-pass (5 passes) optical setup was used to increase the path length through the flame gas (see Fig. 7). This increased the path length through the flame from ≈ 2.5 to ≈ 12 cm for the maximum flame thickness. The beam path was initially positioned vertically at the surface of the pellet, with a portion of the beam path blocked by the HMX pellet. The flame structure and pellet surface location was imaged simultaneously at 60 FPS using a Nikon DSLR camera. This enabled temperature and species measurements to be resolved in time and one dimension as the burning surface receded from the beam path. The beam was then expanded using a second lens telescope to increase the laser beam diameter

such that the beam could be focused to a smaller waist on the spectrograph slit, thereby providing improved spectral resolution. The second telescope consisted of a CaF₂ plano-concave lens ($f = -18$ mm, 2–5 μm AR coating) to expand the laser beam and a CaF₂ plano-convex lens ($f = 100$ mm, 2–5 μm AR coating) to collimate the beam. The input beam had a $1/e^2$ diameter of ≈ 2 mm and an output $1/e^2$ diameter of ≈ 11 mm. A final ZnSe plano-convex cylindrical lens ($f = 50$ mm) focused the beam in one dimension onto the slit of the spectrograph.

4.2 Combustion details

Fireballs of HMX in air were produced as described by Mathews and Goldenstein [38]; however, the most pertinent details will be repeated here for clarity. HMX and HMX-Al test samples were placed in a sample holder located at the bottom of the HPCC. Experiments were conducted with 0.6 g of grade 3 HMX powder, with and without 0.12 g of H-5 micro-aluminum powder (4.5–7.0 μm particle size). The sample holder is a 3-D printed block with a conical cavity to promote ignition and expansion of the fireball. The

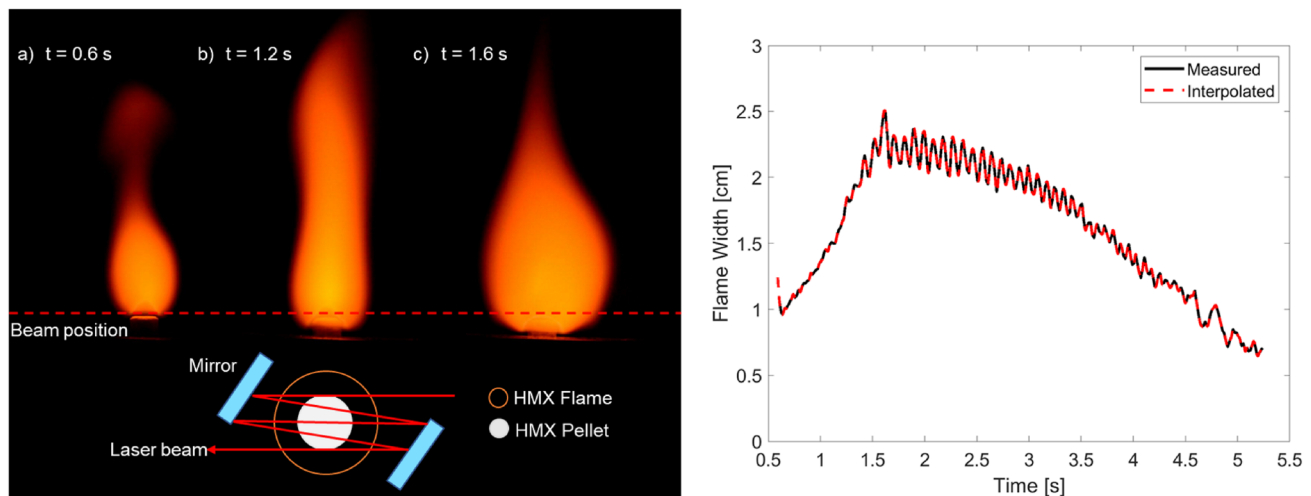


Fig. 7 Images of CO₂-laser-ignited HMX flames (left) and time history of HMX flame width inferred from images (right)

test sample was ignited using an e-match powered by a DC power supply. A 5 cm × 5 cm aluminum baffle plate was placed 15 cm above the sample holder to promote fireball formation and expansion.

In flame experiments, pressed, cylindrical, HMX pellets with a diameter of 6 mm and a height of 4.4 mm were studied. The HMX pellets were ignited using a CO₂ laser (Coherent C-40A) emitting at 10.6 μm. A flux of 78 W/cm² was applied to the surface of the pellet throughout the test duration.

5 Results and discussion

This section presents ULAS measurements of temperature and column densities of CO, NO and H₂O in an HMX flame and HMX fireballs with and without aluminum to demonstrate the measurement capabilities of this diagnostic.

5.1 HMX flame results

5.1.1 Determination of flame width

Figure 7 shows how the flame structure and width evolve in time following laser ignition. Each image (acquired at 60 FPS) was processed using an edge-detection algorithm to determine the flame thickness at the location of the beam path used for ULAS measurements (initially located 6 mm above the pellet surface). A cubic-spline interpolation was used to determine the flame thickness at a rate of 5 kHz to match the ULAS measurement rate. The results illustrate that the width of the flame increases until ≈ 1.6 s (i.e., 1 s after ignition), reaching a maximum value of 2.508 cm. This increase in flame thickness results from expansion of the

flame front across the pellet surface following ignition and, most significantly, the onset of edge burning at $t = 1.15$ s. In addition, at these conditions the flame width oscillates at a frequency of 11.2 Hz which depends on the burn rate and, therefore, parameters which alter it (e.g., laser flux, pressure etc.) [39, 40].

5.1.2 Temperature measurements

In HMX flame experiments, I_0 and I_t were obtained from a single row of pixels within a single image. As a result, measured absorbance spectra were acquired with a projected pixel size of 27 μm which represents a lower bound for the spatial resolution. Temperature measurements with the 95% confidence intervals from the spectral-fitting routine are shown in Fig. 8 as a function of time for measurements acquired in the HMX flame. Prior to ignition, NO absorption lines were observed in the decomposition products above the HMX pellet. The temperature was ≈ 500 K and the NO column density was approximately 0.083 cm. Ignition occurred at $t = 0.59$ s at which point the temperature rapidly increased to 2015 K before quickly decreasing to 1621 K at $t = 0.61$ s which marks the beginning of flame attachment to the surface. Next, a gradual increase in the temperature was observed from 1621 K at $t = 0.61$ s to 2876 K at $t = 1.65$ s. The 95% CI of the temperature measurements was typically 3%. This period of time corresponds to the line of sight (LOS) moving through the near-field (i.e., close to surface) to the far-field equilibrium zone. At quasi-steady state, the time-averaged flame temperature was 2769.43 K with a $1 - \sigma$ precision of 31 K (1% of measurement).

In general, the measured far-field temperature is consistent with prior work; however, several clarifications and distinctions must be made. Tang et al. [39] utilized

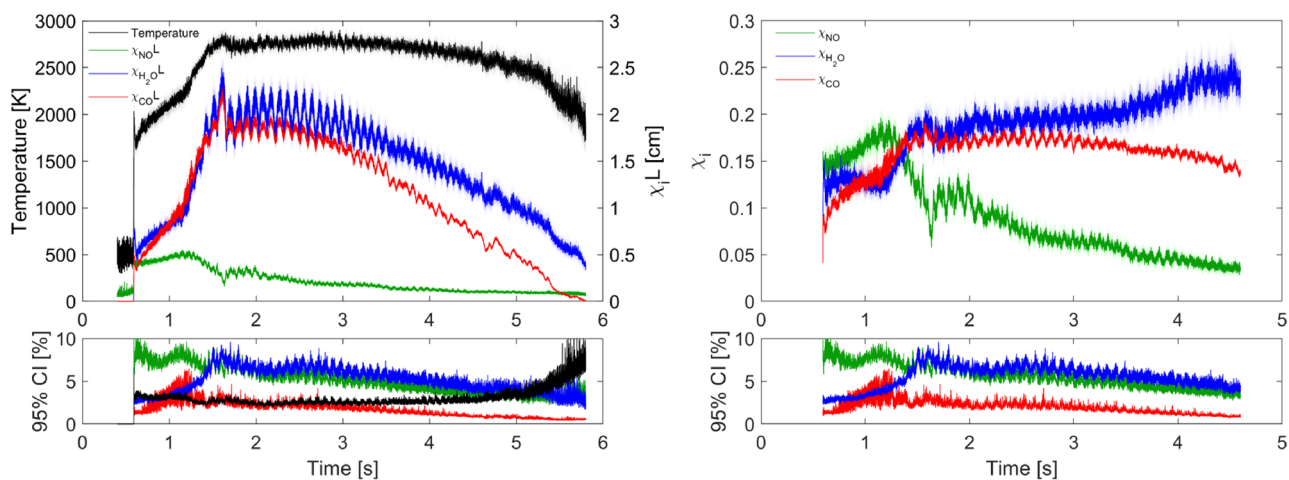


Fig. 8 Time histories of temperature and column density of CO, NO and H₂O in HMX flame (left). Mole fractions of CO, NO and H₂O (right)

thermocouples to measure temperature in HMX flames ignited with a laser flux of 100 W/cm² and observed a gradual increase in temperature in the dark zone of the flame and a final flame temperature of ≈ 2700 K. Parr and Hanson-Parr [41] measured temperature in HMX flames using OH PLIF. HMX pellets were ignited with a laser flux of 628 W/cm² leading to a plateau in the dark zone temperature (≈ 1200 –1500 K) and reported a flame temperature of 2710 K in the equilibrium zone. Note that here, the absence of a temperature plateau in the dark zone is due to the lower laser flux. At lower laser flux, the gas velocity is lower. As a result, the exothermic reactions occur closer to the surface leading to a continuous increase in the temperature [39].

5.1.3 Species measurements

Figure 8 shows the measured time histories of column densities and mole fractions of CO, NO and H₂O. Mole fraction measurements are presented with a 95% CI of 3% for CO measurement and 7% for H₂O and 8% for NO. Ignition occurs at $t = 0.59$ s and the column densities of CO and H₂O increase until reaching peak values of 2.284 cm and 2.495 cm, respectively, at $t = 1.6$ s, where the flame width is maximum in the measurement path, just before reaching quasi-steady state. The column density of NO has a maximum value of 0.548 cm at $t = 1.15$ s which marks the end of the primary reaction zone and the beginning of the secondary reaction zone, where the NO column density decreases rapidly and the CO column density increases. The CO, NO and H₂O column densities have a $1 - \sigma$ precision of 0.8%, 1.8% and 1.6% of measurement, respectively. At quasi-steady state, CO, NO and H₂O column density oscillate at 11.2 Hz which is consistent with the oscillation frequency of the HMX flame at this condition.

These results are mostly consistent with prior work. For example, Tang et al. [39] observed a similar trend in the primary reaction zone, where the mole fractions of NO and H₂O gradually increase with the decrease in concentrations of NO₂, CH₂O, and N₂O. This is followed by the sharp decrease in mole fractions of NO and HCN, and an increase in the mole fractions of CO and N₂. This reaction zone where NO and HCN react to produce CO and N₂ was identified as a key marker for the secondary reaction zone. This observation is better noted in Fig. 8 (right) where mole fractions of CO and H₂O are shown. The mole fractions were calculated (assuming a uniform line of sight) by dividing the column density by the path length which was calculated using Eq. (15).

$$L(t) = D(t) + 2K(t) + \left[\sqrt{(D(t) + K(t))^2 + d^2} \right], \quad (15)$$

$$K(t) = \left(\sqrt{D(t)^2 - d^2} \right).$$

Here, $L(t)$ (cm) is the path length, $D(t)$ is the instantaneous flame width, and d is the initial pellet diameter. This equation was derived for the optical path geometry shown in Fig. 7. It assumes that the mirrors are close to the outer edge of the flame such that the pulses reflect at the flame boundary. The reflections are positioned such that the first and last pass of a pulse through the flame is tangential to the outer edge of the pellet. The third pass of the pulse is through the center of the flame. This equation is valid only for $D(t) \geq d$.

However, for the calculation of NO mole fraction, the path length was approximated as a constant value of 2 cm. This approximation was made based on prior work by researchers [39, 41, 42] who concluded that NO is primarily formed due to the reactions which occur close to the surface of the pellet. Therefore the path length for NO was

calculated by considering only the width of the dark zone region and three laser passes through it. At $t = 0.59$ s and 0.6 mm above the surface, mole fractions of CO, NO and H₂O are 0.07, 0.14, and 0.15, respectively. The mole fraction of NO rises to a maximum value of 0.195 at $t = 1.15$ s in the primary reaction zone. After which, the NO mole fraction falls, with a corresponding increase in CO and H₂O concentrations. Close to $t = 1.6$ s, the mole fractions of CO, H₂O, and NO at the beginning of quasi-steady state combustion are 0.191, 0.204 and 0.057, respectively, which is consistent with the results reported in the literature [23, 39]. NO and H₂O mole fractions exhibit trends that agree with the work of Tang et al. [39] and Paletsky et al. [42]. At $t \approx 1.8$ s, the NO mole fraction increases with a slight decrease in CO and H₂O as the mixture shifts towards equilibrium. This effect was also observed by Paletsky et al. [42]. Next as time progresses beyond 1.8 s, the flame continues to propagate downwards, and an increase in the H₂O concentration is accompanied by a decrease in CO concentration. This trend continues and ultimately results from air entrainment into the fuel-rich product plume which leads to additional H₂O and oxidation of CO to CO₂.

5.2 HMX fireball results

Simultaneous measurements of temperature and column densities of CO, NO, and H₂O were acquired in HMX fireballs to demonstrate the diagnostic's ability to characterize harsh, particulate laden, transient combustion events with high precision.

5.2.1 Temperature measurements

Figure 9 presents measured time histories of temperature and column density acquired in HMX fireballs with and without

the addition of micro-aluminum. In both cases, the harsh particulate-laden environment caused a significant decrease in the transmitted light intensity. As a result, approximately 20 adjacent rows of spectra were averaged for each laser shot to improve the SNR. This led to the spectra being averaged across a ≤ 1 mm region (transverse to line of sight) within the fireball.

For the HMX fireballs without aluminum, the temperature peaks near 2820 K at $t = 67.3$ ms and then begins to decrease at approximately $t = 170.5$ ms. The $1 - \sigma$ measurement precision at the temperature plateau is 11 K (0.4% of measurement) and the 95% CI is 2.5%. For the aluminumized HMX fireballs, the peak path-integrated temperature was 2871 K and this was observed shortly after the fireball reached the measurement path ($t = 29.1$ ms). The temperature remained above 2000 K for a duration of 290 ms which is three times longer than that observed in the pure HMX fireballs. This trend is consistent with results acquired previously in our lab [38], and this likely results simply from the fact that the aluminum particles require more time to burn. The $1 - \sigma$ measurement precision is 7.8 K (i.e., 0.3% of measurement) and the 95% CI is 2% of the measurement value.

5.2.2 Species measurements

For the pure HMX fireball, following ignition, the column density of all three species rapidly increases with that of NO peaking first, followed by H₂O and CO which peak near simultaneously. The column densities of NO and H₂O exhibit trends similar to that of the temperature profile, reaching a maximum value of 1.733 cm and 2.362 cm at $t = 55.7$ ms and $t = 76.9$ ms, respectively. The column densities start decreasing at $t = 170.5$ ms as the fireball size decreases and combustion products rise out of the test chamber. The

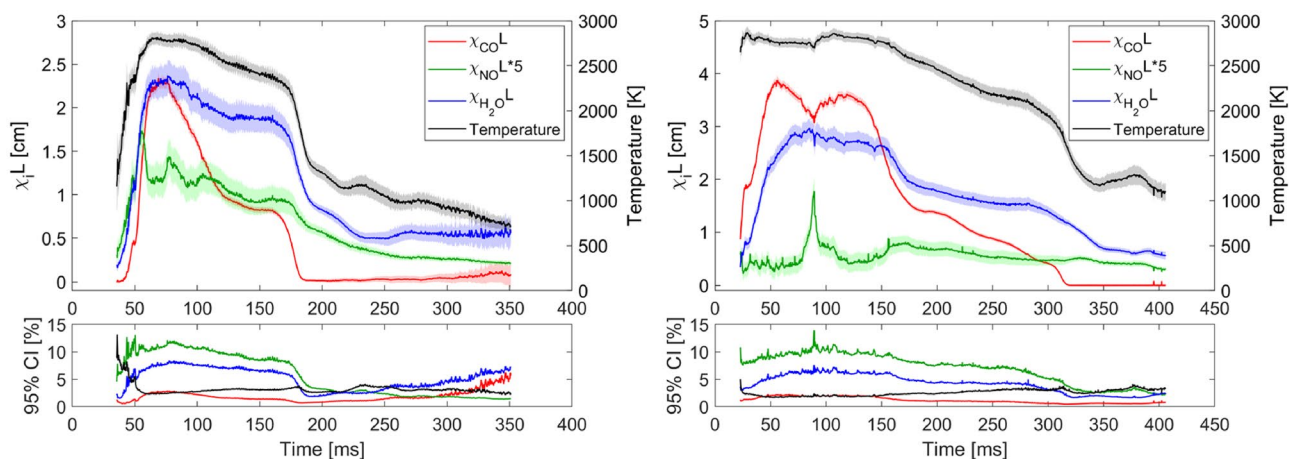


Fig. 9 Measured time histories of temperature and column densities of CO, NO, and H₂O acquired in HMX fireballs without (left) and with (right) micro aluminum

CO column density increases rapidly to a maximum value of 2.336 cm at $t = 69.1$ ms. The column density of CO decreases earlier ($t \approx 78.3$ ms) as CO is oxidized to CO_2 due to air entrainment. The column density measurements are presented with a 95% CI of 2.5% for CO, 7% for H_2O , and 11% for NO. The $1 - \sigma$ measurement precision is 0.3% for CO, 0.5% for H_2O , and 0.6% for NO.

For aluminized HMX fireballs, the column density of CO reaches a maximum value of 3.872 cm at $t = 56.3$ ms and the column density remains elevated for a longer period of time compared to the pure HMX fireball. The column density of H_2O peaks at 2.96 cm at $t = 84.9$ ms and decreases with decreasing temperature at $t \approx 320$ ms. In contrast, the column density of NO is significantly lower compared to pure HMX fireballs, however, a peak of 1.774 cm occurs at $t \approx 89.5$ ms which is accompanied by a sudden dip in CO column density and a decrease in the transmitted light intensity at non-resonant wavelengths. These results suggest there is unburnt HMX particles in the LOS. The 95% CI of CO column densities are within 2% of the measurement value, while H_2O and NO column densities are within 7% and 11%, respectively. The $1 - \sigma$ precision for CO, NO and H_2O are 0.2%, 0.15% and 0.37%, respectively.

For a path length of ≈ 19 cm, the maximum mole fractions of H_2O are 0.15 and 0.12 for HMX fireballs with and without microaluminum, respectively. These results exhibit good agreement with results presented in Ref. [38] where measurements were made in fireballs of energetic materials using a WMS-based diagnostic. Measurements made in fireballs with lower amounts of HMX and similar percentage of aluminum also exhibited similar trends. The formation of $\approx 2 \times$ the amount of CO in fireballs with microaluminum was consistently observed in all cases. Figure 10 shows the ratio of CO to H_2O formed in fireballs with and without aluminum. The addition of aluminum leads to larger amounts of CO since CO_2 is the primary oxidizer of aluminum for the fuel-rich formulations tested. This also follows from the work of Bazyn et al. [43] who showed that for 10 μm aluminum particles, the burn rate is greater in a CO_2 bath compared to in an H_2O bath.

6 Conclusion

The design and application of a novel ultrafast-laser-absorption-spectroscopy diagnostic for simultaneous, single-shot, multi-species and temperature measurements in HMX combustion gases were presented. Time-resolved measurements of temperature and column densities of CO, NO and H_2O were acquired in HMX flames and fireballs of HMX with and without the addition of micro aluminum. The results demonstrate that this diagnostic can provide high-precision

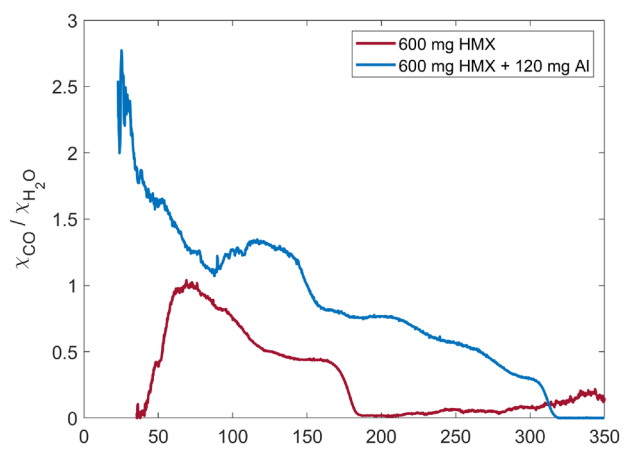


Fig. 10 Mole fraction ratio ($\text{CO}:\text{H}_2\text{O}$) as a function of time in fireballs with and without micro aluminum

measurements with ultrafast time-resolution through the use of broadband, mid-infrared pulses at a repetition rate of 5 kHz.

The temperature and mole fraction measurements acquired in an HMX flame agree well with those reported previously in the literature, thereby supporting the accuracy of the diagnostic. Further, measurements acquired in HMX fireballs illustrate the ability of this diagnostic to characterize fireball chemistry via multi-species time histories. In particular, the measurements of CO illustrate the impact of aluminum addition and provide insight regarding the time-scale of air entrainment.

Collectively, these results demonstrate that ULAS can be utilized to provide ultrafast, multi-parameter characterization of a wide variety of harsh combustion environments involving energetic materials.

Acknowledgements This work was supported by AFOSR Grant FA9550-18-1-0210 and DTRA Grant HDTRA1-17-1-0023. The authors thank Dr. Mingming Gu for his help operating the ultrafast laser system during the course of this work and Prof. Robert Lucht for helping support the operation of the ultrafast laser

References

1. C.S. Goldenstein, R.M. Spearrin, J.B. Jeffries, R.K. Hanson, Infrared laser-absorption sensing for combustion gases. *Prog. Energy Combust. Sci.* **60**, 132–176 (2017)
2. C. Murzyn, A. Sims, H. Krier, N. Glumac, High speed temperature, pressure, and water vapor concentration measurement in explosive fireballs using tunable diode laser absorption spectroscopy. *Opt. Lasers Eng.* **110**, 186–192 (2018)
3. W.Y. Peng, S.J. Cassady, C.L. Strand, C.S. Goldenstein, R.M. Spearrin, C.M. Brophy, J.B. Jeffries, R.K. Hanson, Single-ended mid-infrared laser-absorption sensor for time-resolved measurements of water concentration and temperature within the annulus of a rotating detonation engine. *Proc. Combust. Inst.* **37**(2), 1435–1443 (2019)

4. S.J. Cassady, W.Y. Peng, C.L. Strand, D.F. Dausen, J.R. Codoni, C.M. Brophy, R.K. Hanson, Time-resolved, single-ended laser absorption thermometry and H₂O, CO₂, and CO speciation in a H₂/C₂H₄-fueled rotating detonation engine. *Proc. Combust. Inst.* **38**(1), 1719–1727 (2021)
5. K.D. Rein, S. Roy, S.T. Sanders, A.W. Caswell, F.R. Schauer, J.R. Gord, Multispecies absorption spectroscopy of detonation events at 100 kHz using a fiber-coupled, time-division-multiplexed quantum-cascade-laser system. *Appl. Opt.* **55**(23), 6256–6262 (2016)
6. X. An, A.W. Caswell, S.T. Sanders, Quantifying the temperature sensitivity of practical spectra using a new spectroscopic quantity: frequency-dependent lower-state energy. *J. Quant. Spectrosc. Radiat. Transf.* **112**(5), 779–785 (2011)
7. C.S. Goldenstein, C.A. Almodovar, J.B. Jeffries, R.K. Hanson, C.M. Brophy, High-bandwidth scanned-wavelength-modulation spectroscopy sensors for temperature and H₂O in a rotating detonation engine. *Meas. Sci. Technol.* **25**(10), 105104 (2014)
8. S.T. Sanders, J. Wang, J.B. Jeffries, R.K. Hanson, Diode-laser absorption sensor for line-of-sight gas temperature distributions. *Appl. Opt.* **40**(24), 4404–4415 (2001)
9. K.D. Rein, S. Roy, S.T. Sanders, A.W. Caswell, F.R. Schauer, J.R. Gord, Measurements of gas temperatures at 100 kHz within the annulus of a rotating detonation engine. *Appl. Phys. B* **123**(3), 88 (2017)
10. C.L. Strand, Y. Ding, S.E. Johnson, R.K. Hanson, Measurement of the mid-infrared absorption spectra of ethylene (C₂H₄) and other molecules at high temperatures and pressures. *J. Quant. Spectrosc. Radiat. Transf.* **222**, 122–129 (2019)
11. S.T. Sanders, Wavelength-agile fiber laser using group-velocity dispersion of pulsed super-continua and application to broadband absorption spectroscopy. *Appl. Phys. B* **75**(6–7), 799–802 (2002)
12. N. Göran Blume, S. Wagner, Broadband supercontinuum laser absorption spectrometer for multiparameter gas phase combustion diagnostics. *Opt. Lett.* **40**(13), 3141–3144 (2015)
13. P.J. Schroeder, R.J. Wright, S. Coburn, B. Sodergren, K.C. Cossel, S. Droste, G.W. Truong, E. Baumann, F.R. Giorgetta, I. Coddington et al., Dual frequency comb laser absorption spectroscopy in a 16 MW gas turbine exhaust. *Proc. Combust. Inst.* **36**(3), 4565–4573 (2017)
14. N. Glumac, Absorption spectroscopy measurements in optically dense explosive fireballs using a modeless broadband dye laser. *Appl. Spectrosc.* **63**(9), 1075–1080 (2009)
15. M. Soo, N. Glumac, Ultraviolet absorption spectroscopy in optically dense fireballs using broadband second-harmonic generation of a pulsed modeless dye laser. *Appl. Spectrosc.* **68**(5), 517–524 (2014)
16. J.R. Carney, J.M. Lightstone, S. Picuch, J.D. Koch, Water temperature and concentration measurements within the expanding blast wave of a high explosive. *Meas. Sci. Technol.* **22**(4), 045601 (2011)
17. M.C. Phillips, B.E. Bernacki, S.S. Harilal, B.E. Brumfield, J.M. Schwallier, N.G. Glumac, Characterization of high-explosive detonations using broadband infrared external cavity quantum cascade laser absorption spectroscopy. *J. Appl. Phys.* **126**(9), 093102 (2019)
18. A.C. LoCurto, M.A. Welch, T.R. Sippel, J.B. Michael, High-speed visible supercontinuum laser absorption spectroscopy of metal oxides. *Opt. Lett.* **46**(13), 3288–3291 (2021)
19. M.A. Zamkov, R.W. Conner, D.D. Dlott, Ultrafast chemistry of nanoenergetic materials studied by time-resolved infrared spectroscopy: aluminum nanoparticles in teflon. *J. Phys. Chem. C* **111**(28), 10278–10284 (2007)
20. P. Bowlan, M. Powell, R. Perriot, E. Martinez, E.M. Kober, M.J. Cawkwell, S. McGrane, Probing ultrafast shock-induced chemistry in liquids using broad-band mid-infrared absorption spectroscopy. *J. Chem. Phys.* **150**(20), 204503 (2019)
21. Z.E. Loparo, E. Ninnemann, Q. Ru, K.L. Vodopyanov, S.S. Vasu, Broadband mid-infrared optical parametric oscillator for dynamic high-temperature multi-species measurements in reacting systems. *Opt. Lett.* **45**(2), 491–494 (2020)
22. H.U. Stauffer, P.S. Walsh, S. Roy, J.R. Gord, Time-resolved optically gated absorption (TOGA) spectroscopy: A background-free, single-shot broadband absorption method for combustive flows, in *AIAA Scitech 2019 Forum*, p. 1607 (2019)
23. R.J. Tancin, Z. Chang, M. Gu, V. Radhakrishna, R.P. Lucht, C.S. Goldenstein, Ultrafast laser-absorption spectroscopy for single-shot, mid-infrared measurements of temperature, CO, and CH₄ in flames. *Opt. Lett.* **45**(2), 583–586 (2020)
24. R.J. Tancin, C.S. Goldenstein, Ultrafast-laser-absorption spectroscopy in the mid-infrared for single-shot, calibration-free temperature and species measurements in low- and high-pressure combustion gases. *Opt. Express* **29**(19), 30140–30154 (2021)
25. R.J. Tancin, Z. Chang, V. Radhakrishna, M. Gu, R.P. Lucht, C.S. Goldenstein, Ultrafast laser absorption spectroscopy in the mid-infrared for measuring temperature and species in combustion gases, in *AIAA Scitech 2020 Forum*, p. 0517 (2020)
26. X. Zhou, J.B. Jeffries, R.K. Hanson, Development of a fast temperature sensor for combustion gases using a single tunable diode laser. *Appl. Phys. B* **81**(5), 711–722 (2005)
27. R.K. Hanson, R.M. Spearrin, C.S. Goldenstein, *Spectroscopy and optical diagnostics for gases* (Springer, Switzerland, 2016)
28. C.S. Goldenstein, V.A. Miller, R.M. Spearrin, C.L. Strand, Spectraplot. com: integrated spectroscopic modeling of atomic and molecular gases. *J. Quant. Spectrosc. Radiat. Transf.* **200**, 249–257 (2017)
29. L.S. Rothman, I.E. Gordon, R.J. Barber, H. Dothe, R.R. Gamache, A. Goldman, V.I. Perevalov, S.A. Tashkun, J. Tennyson, HITEMP, the high-temperature molecular spectroscopic database. *J. Quant. Spectrosc. Radiat. Transf.* **111**(15), 2139–2150 (2010)
30. G. Li, I.E. Gordon, L.S. Rothman, Y. Tan, S.-M. Hu, S. Kassi, A. Campargue, E.S. Medvedev, Rovibrational line lists for nine isotopologues of the CO molecule in the X¹Σ⁺ ground electronic state. *Astrophys. J. Suppl. Ser.* **216**(1), 15 (2015)
31. HITRANonline (2010), <https://hitran.org/hitemp/>. Accessed 10 Feb 2020
32. R.J. Hargreaves, I.E. Gordon, L.S. Rothman, S.A. Tashkun, V.I. Perevalov, A.A. Lukashchinskaya, S.N. Yurchenko, J. Tennyson, H.S.P. Müller, Spectroscopic line parameters of NO, NO₂, and N₂O for the HITEMP database. *J. Quant. Spectrosc. Radiat. Transf.* **232**, 35–53 (2019)
33. C.S. Goldenstein, R.K. Hanson, Diode-laser measurements of linewidth and temperature-dependent lineshape parameters for H₂O transitions near 1.4 μm using Voigt, Rautian, Galatry, and speed-dependent Voigt profiles. *J. Quant. Spectrosc. Radiat. Transf.* **152**, 127–139 (2015)
34. A.P. Nair, D.D. Lee, D.I. Pineda, J. Kriesel, W.A. Hargus, J.W. Bennowitz, S.A. Danczyk, R.M. Spearrin, MHz laser absorption spectroscopy via diplexed RF modulation for pressure, temperature, and species in rotating detonation rocket flows. *Appl. Phys. B* **126**(8), 1–20 (2020)
35. S.I. Sandler, J.K. Wheatley, Intermolecular potential parameter combining rules for the Lennard-Jones 6–12 potential. *Chem. Phys. Lett.* **10**(4), 375–378 (1971)
36. A.W. Jasper, J.A. Miller, Lennard-Jones parameters for combustion and chemical kinetics modeling from full-dimensional intermolecular potentials. *Combust. Flame* **161**(1), 101–110 (2014)
37. R.J. Tancin, G.C. Mathews, C.S. Goldenstein, Design and application of a high-pressure combustion chamber for studying propellant flames with laser diagnostics. *Rev. Sci. Instrum.* **90**(4), 045111 (2019)
38. G. Mathews, C. Goldenstein, Near-GHz scanned-wavelength-modulation spectroscopy for MHz thermometry and H₂O

- measurements in aluminized fireballs of energetic materials. *Appl. Phys. B* **126**(11), 1–17 (2020)
39. C.-J. Tang, Y.J. Lee, G. Kudva, T.A. Litzinger, A study of the gas-phase chemical structure during CO₂ laser assisted combustion of HMX. *Combust. Flame* **117**(1–2), 170–188 (1999)
40. J.C. Finlinson, T. Parr, D. Hanson-Parr, Laser recoil, plume emission, and flame height combustion response of HMX and RDX at atmospheric pressure, in *Symposium (international) on combustion*, vol. 25 (Elsevier, 1994), pp. 1645–1650
41. T.P. Parr, D. Hanson-Parr, Solid propellant flame chemistry and structure. *Int. J. Energ. Mater. Chem. Propul.* **3**(1–6), 571–599 (1994)
42. A.A. Paletsky, E.N. Volkov, O.P. Korobeinichev, HMX flame structure for combustion in air at a pressure of 1 atm. *Combust. Explos. Shock Waves* **44**(6), 639–654 (2008)
43. T. Bazyn, H. Krier, N. Glumac, Oxidizer and pressure effects on the combustion of 10-micron aluminum particles. *J. Propul. Power* **21**(4), 577–582 (2005)

Publisher's Note Springer Nature remains neutral with regard to jurisdictional claims in published maps and institutional affiliations.